Experimental Study of Particle Migration in Polymer Processing

José Luis Colón Quintana , ** Tobias Heckner, Achim Chrupala, Jesse Pollock, Sebastian Goris, ** Tim Osswald

¹Polymer Engineering Center, Department of Mechanical Engineering University of Wisconsin-Madison, Madison, Wisconsin, 53706-1691

Extrusion and injection molding processes of filled polymers are widely used in industry due to their high strength-to-weight ratios and for their ability to manufacture a variety of geometries while improving the overall mechanical and thermal properties. However, filler migration and filler-matrix separation during processing are phenomena that are not fully understood. To gain an improved understanding of these phenomena, polypropylene samples with different glass bead concentrations were manufactured using extrusion, injection molding and a customized screwless extruder that was built in-house. Computed tomography was performed on the samples to observe particle position and distribution after material solidification.

For all three processes, filler migration and filler–matrix separation was observed. In the extrusion and screwless extrusion processes, particles migrated towards the wall, contrary to current theories and believes. During the injection molding process, filler–matrix separation was manifested as bead-free zones in the center region and the walls of the spiral mold at the entrance region of the spiral mold. These bead-free zones were later filled at the far end of the spiral mold suggesting migration of particles along flow with almost no bead-free zones at the end of the mold. Particle redistribution towards the wall and the center during flow could possibly have happened due to migration and fountain flow effects. POLYM. COMPOS., 40:2165–2177, 2019. © 2018 Society of Plastics Engineers

INTRODUCTION

Extrusion and injection molding processes of filled polymers are widely used manufacturing techniques in the polymer industry due to their ability to manufacture a wide variety of geometries with high strength to weight rations.

Additional Supporting Information may be found in the online version of this article.

Correspondence to: J. L. Colón Quintana; e-mail: colonquintan@wisc.edu DOI 10.1002/pc.25018

Published online in Wiley Online Library (wileyonlinelibrary.com). © 2018 Society of Plastics Engineers

To strengthen the overall mechanical and thermal properties of these products, fillers are used to reinforce the polymeric matrix. Fillers can be spherical particles or fibers as well as a combination of both [1]. The process-induced microstructure of the reinforcing phase affects the final properties and performance of the manufactured part. Processing conditions that affect the performance are processing temperature, processing speed, filler concentration, aspect ratio of fillers and part geometry. During processing of filled polymers, the filler and matrix often start to separate, leading to filler density distributions within the manufactured part [2,3]. As a result of fillers migrating to undesired positions within the manufactured part, failure or weakening of the composite can occur.

One of the most common phenomenons seen in literature [4-6] is the filler-matrix separation and shear-induced migration. Suspension rheology of monodisperse particles embedded in low viscosity Newtonian fluids has been studied in the last century to understand this behavior. Segré and Silberberg [7] were the first who observed particle migration during Poiseuille flow. They observed that particles migrate during flow reaching an equilibrium position at about 0.6 of the tube radius as a result of radially acting forces. Many continuum models have been proposed to estimate the behavior of the particles within a flow [4,8–15]. Some study scenarios are particles under sedimentation [16], under an incline wall [17], using Poiseuille flow and other rheometric flows [5,6,18-25], and in polymer blends [27–30]. Some authors debate either the magnitude of the first and second normal stresses or the direction of these normal stresses influence the direction of the filler migration [26,31]. The behavior of the particles varies according to the type of carrier fluid, Newtonian versus Non-Newtonian [32,33]. It has also been reported that the viscosity [34,35] of the fluid and the shear rate [36] influence the direction of the migration of the particles. Other characteristics that can affect the direction of migration of particles is the particle concentration. This influences the

²Robert Bosch GmbH, Corporate Research and Advance Engineering, 71272, Renningen, Germany

particle-particle interactions as well as the size of the particles, which also affects the interaction forces as well as the hydrodynamic forces during flow [21,37].

For this purpose, the effects of filler migration in extrusion and injection molding process were investigated. Furthermore, the effects of filler migration in a polymer melt through a screwless extruder was studied to eliminate the effects from the screw during processing. For both, the extrusion and injection molding process, a customized die was manufactured allowing full control of the material after solidification. The screwless extruder will help to understand particle migration during a cone contraction. The current background is still being debated in terms of what is happening during processing of particle-reinforced thermoplastics. This study will help to improve the understanding of particle migration during polymer processing and better understand how this migration affects the final properties of parts produced using these materials.

EXPERIMENTAL

Materials

The material used for the experiments is a polypropylene (PP) matrix embedded with glass beads (GBs) from RTP Company (Winona, MN) named RTP 100. The GB particles range from 20 to 50 μ m diameter with a density of $\rho = 2.55$ g/cm³. Composition of the materials used were 10, 20 and 40 wt% GB. According to the supplier, the processing temperature of the pelletized material ranges between 190.6 and 232.2°C (375–450°F). For analysis purposes, each weight percentage was converted to volume percentage (vol%) as shown in Table 1.

Extrusion Process

Equipment and Specifications. For this experiment a 25.4 mm (1 inch) single screw extruder from Davis Standard Corporation (DS-10H) was used. The extruder is a plasticating extruder with three heating zones, possesses a gear ratio of 12.8, reaches a maximum of 100 RPM and has an output of 14.9 kW. The extruder is located in the facilities of Teel Plastics Inc, shown in Fig. 1.

The depth of the channel in the solid conveying zone and the pumping zone of the channel are 4.95 and 1.80 mm, respectively. The extruder has a multi-flight screw, which leads to a continuous reduction in the width of the solid channel. This reduction increases the width of the melt channel as seen in Fig. 2a. This geometry allows a

TABLE 1. GB weight percentage and volume fraction.

Material	GB 10	GB 20	GB 40
GB wt%	10	20	40
GB vol%	3.81	8.19	19.22

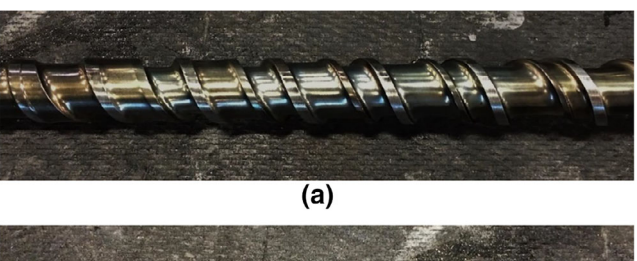


FIG. 1. Davis Standard Corporation (DS-10H) single screw extruder. [Color figure can be viewed at wileyonlinelibrary.com]

smooth and gradual change of the solid channel as well as the melt channel [38]. At the end of the screw a 55.88-mm long fluted mixer is located (Fig. 2b).

Customized Die. The customized die consists of a cylindrical-shaped rod with a diameter of 6.35 mm and a length of 300 mm, respectively. A schematic of the die is shown in Fig. 3. The design consists of a two-part mold for easy removal of samples. Two valves are located in the die, one at the inlet and one at the outlet to control the flow. Each valve can be controlled individually allowing the flow of the melted polymer inside the die to be stopped at any given time. The first valve of the die (inlet) is designed to accomplish two functions. With an open valve, the melt can flow inside of the die. When the valve is closed, the melt is redirected to a bottom orifice. With this valve, it is possible to control the flow of the melt at the inlet position.

A total of 12 cartridge heaters were used to maintain a constant temperature through the complete die. Two



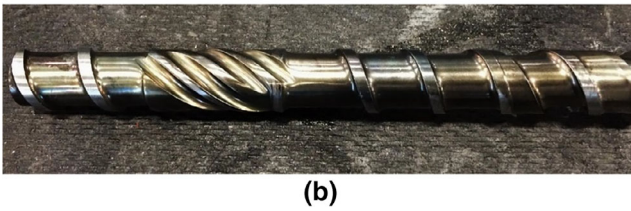


FIG. 2. Davis Standard Corporation (DS-10H) single screw extruder geometry of (a) screw and (b) fluted mixer. [Color figure can be viewed at wileyonlinelibrary.com]

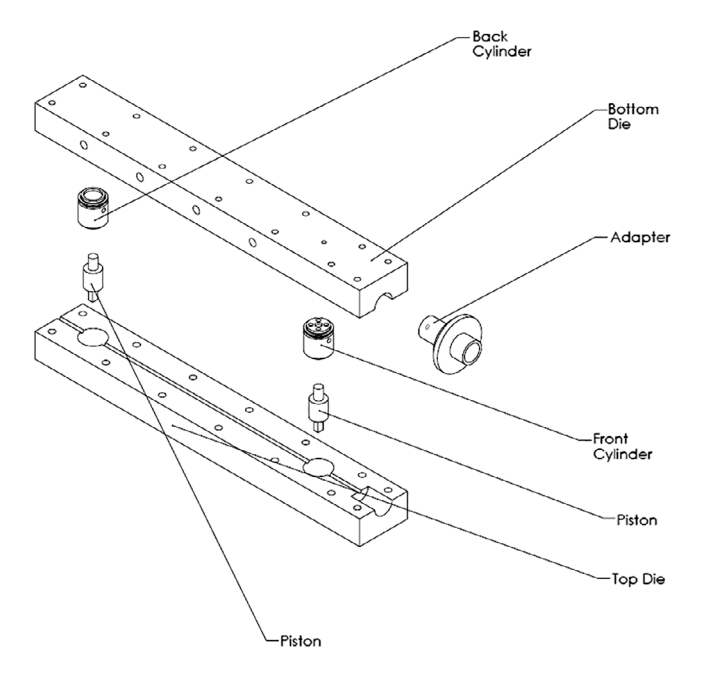


FIG. 3. Sketch of customized die for extrusion process.

thermocouples were used to measure the temperature of the die, one at the entrance and one at the exit of the die.

Experimental Procedure. To analyze the average particle density distribution of the particles through the process, samples were collected at different sections of the extrusion process. The temperature profile of the extruder is shown in Fig. 4b. Sampling locations include the pellets, extrudate, cone inlet, cone outlet, die inlet, and die outlet as shown in Fig. 4a. Samples with a concentration of 10, 20, and 40 wt% GB were manufactured. Screw speeds of 10 and 20 RPM were used to study the particle migration

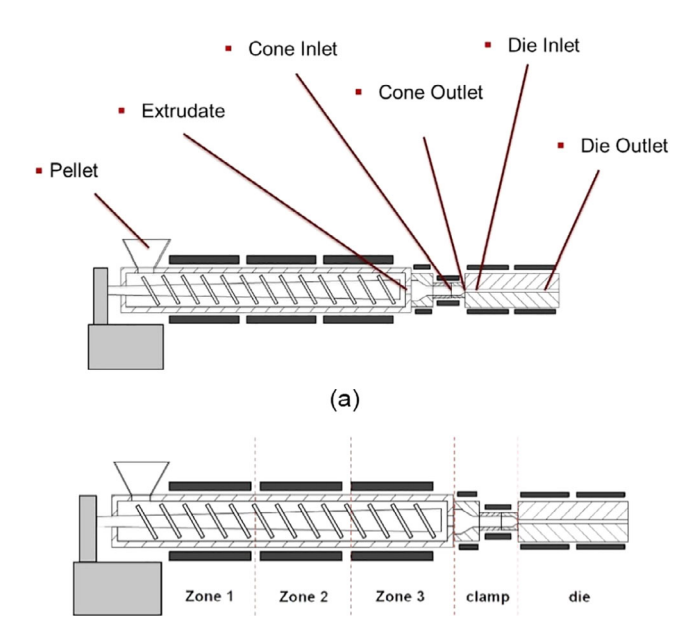


FIG. 4. Sketch of (a) sample selection in extrusion process and (b) temperature zones (187.8 C in Zone 1, 193.3°C in Zone 2, 198.9°C in Zone 3, and 204.4°C in the clamp and die).

under different shear stress levels. All samples were collected once steady state conditions were reached.

Injection Molding Process

Equipment and Specifications. For this experiment, samples were manufactured using an Arburg 270 A injection molding machine. The screw diameter was 18 mm with an effective screw length to diameter (*L/D*) of 24.5. The maximum stroke volume is 23 cm³, which results in a shot weight of approximately 23.9 g. The maximum injection pressure and speed are 250 MPa (2,500 bar) and 76 cm³/s, respectively. The maximum nozzle contact force is 50 kN (5.62 Ton).

Customized Spiral Die. The customized die consists of a circular 5-mm diameter spiral mold with a total length of 1,724 mm as shown in Fig. 5. The sprue bushing is in the center and the spiral surrounds the sprue. The melt is transported into the cavity via a tapered sprue gate design. The mold is split along the center of the cavity into two parts. Side A describes the plate which is closer to the sprue while side B designates the rest of the mold. In side B there is a small indentation that makes it easier to demold the spiral after cooling.

Experimental Procedure. The spiral was manufactured using PP with 20 and 30 wt% GB. A melt temperature of 280 °C was used as processing temperature in order to be able to fully fill the mold. Injection speed, mold temperature and injection volume used were 49.9 cm³/s, 80°C and 20 cm³, respectively. The holding pressure and back pressure were set to 44 and 1.2 MPa, respectively. The spiral was cut into 35 mm samples at three positions. Position 1 is closest to the sprue, Position 2 is at the center of the spiral mold and Position 3 is the furthest along the spiral.

Screwless Extruder

Equipment and Specification. For this experiment, samples were manufactured using a device built in house. To remove any effect involving the extruder screw, the design consisted of three sections as shown in Fig. 6. Introduction section consists of a melting barrel with inside and outside diameter of 25.4 mm (1 in) and 50.8 mm (2 inches), respectively. Experimental section is a cone shaped contraction with inlet and outlet diameter of 25.4 and 12.7 mm (0.5 in. and a cone angle $\alpha = 57^{\circ}$, respectively. Results and Discussion section consists of a die with an inside diameter of 12.7 mm and outside diameter of 38.1 mm (1.5 in). The sections are fitted together using a threaded connection.

Customized Equipment. The customized equipment consists of a screwless extruder with three sections as described above. Premium MICA heater bands from PPE Molding Accessories Catalog were placed around the three

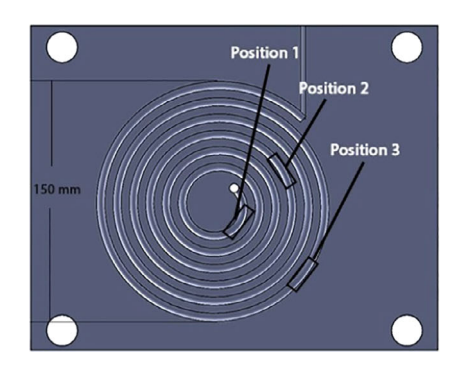




FIG. 5. Spiral mold design. [Color figure can be viewed at wileyonlinelibrary.com]

sections as shown in Fig. 7. Heater dimensions and properties are shown in Table 2.

Electronic PID INKBIRD temperature controllers (INKBIRD Tech, Co., Ltd model ITC- 106VH), SSR-40 DA solid state module and K-Type thermocouples were used to measure the system temperature, allowing a constant temperature in each section. A total of four heaters were used for the device, two for the melting barrel and one in both the cone and die sections. A pneumatic system was implemented to actuate a piston and initiate flow. The pneumatic piston is a PHD Tom Thumb cylinder series HV B (10.34 MPa [1,500 psi] Hyd. with bottom mount, tapped holes in head and cap) from PHD, Inc. (Fort Wayne, IN) with a bore size of 28.575 mm (1.125 in. and a stroke length of 139.7 mm (5.5 in). A mechanical energy balance was used to determine the pressure as a function of the flow velocity of the system. COMSOL Multiphysics, a commercial simulation software, was used to perform a 1D thermal analysis of the system. A total of 10.5 minutes are required for the polymer to melt and reach the target temperature.

Experimental Procedure. The experiment was performed by filling the screwless extruder (barrel, cone and die) entirely with 20 wt% GB polymer pellets. Three pressure levels were selected: 344.7, 517.1, and 689.5 kPa (50, 75, and 100 psi). The air pressure supply of the research facility limited the pressure used. The test was performed under isothermal condition, all sections were maintained at 204.4°C (400°F). The effect of processing speed was studied to understand the influence of flow velocity on the particle migration. A total time of 11 min was given to the system to allow melting of the polymer. After melting the polymer, a piston connected to the compressed air was used to push the molten polymer through the screwless extruder. Afterwards, the samples at the cone were collected and analyzed further.



FIG. 6. Cross-section view of the screwless extruder.

Thermal Gravimetrical Analysis

To ensure the polymer was not suffering thermal degradation during the heating process of the material, thermogravimetric analysis (TGA) was performed to measure the thermal degradation of the polymeric matrix at different processing temperatures. A temperature ramp of 20 K/min was set with a final temperature of 200, 250, and 300°C for 1 h. Samples with 10, 20, and 40 wt% GB were submitted to an atmosphere of nitrogen (N2) and air to allow oxidation.

As shown in Fig. 8a, c, and e, negligible thermal degradation was observed for samples at a constant temperature of 200, 250, and 300°C, respectively. Samples were subjected to a nitrogen atmosphere and showed a maximum decrease of 1 and 2 mass percentage for the samples at 250 and 300°C respectively. For samples subjected to an air atmosphere, considerable thermal degradation was observed as shown in Fig. 8b, d, and f. For a constant temperature of 200°C significant thermal degradation started after 40 min with a maximum decrease of 10 mass percentage for the sample with 20 wt% GB. For samples at a constant temperature of 250 and 300°C, the results show significant thermal degradation after 15 min with a maximum decrease of 50 mass percentage for samples subjected to 250°C and a maximum decrease of 80 mass percentage at 300°C. The presence of oxygen increases the degradation rate by decomposing and oxidizing the polymer [39]. However, as seen in Fig. 8, no thermal degradation occurred within our manufacturing processes as a result of the low residence time.

Image Processing

Computed Tomography—CT Scan. A ZEISS METROTOM 800 (ZEISS, Germany) was used for the

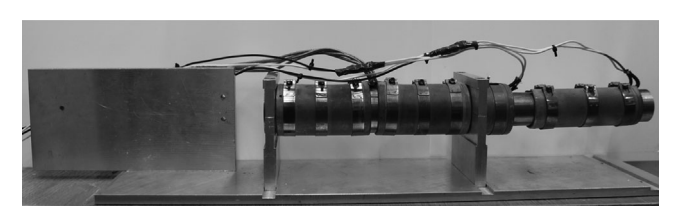


FIG. 7. Position of heater bands.

TABLE 2. Heater Band Specifications.

Quantity	Inside diameter (in)	Width (in)	Volts (V)	Watts (W)	Heat Flux (W) m2
1	1.5	5	120	700	46,048.92
2	2	4	120	800	49,338.13
1	2	1.5	120	300	65,784.17

computed tomography of the samples. Samples were cut and scanned from each section as mentioned earlier. To test the dispersion of the GBs and the uniformity of the concentration in the feed material, the raw pellets were also scanned. Table 3 shows the parameters used to obtain high quality scans. The μ CT data comprises a 3D reconstruction of the scanned sample, which is exported to 2D image stacks. The two phases (filler and matrix) can be clearly distinguished in the grayscale images. For the image processing and concentration quantification, the grayscale images were converted to binary images through global thresholding.

Image Processing Software. ImageJ, an open source image processing software, was used as the tool to analyze the ZEISS METROTOM 800 output data. The image type was selected to 16-bit unsigned, the width, height, offset to first image and number of images were selected according the output file (image dimension), and the little-endian byte order was enable. A MATLAB script was used to analyze the images as shown in Fig. 9. Each image was imported to the workspace using the imread function (Fig. 9a). Afterwards, imadjust function (Fig. 9b) was used to map the intensity values in grayscale. Next, the imsharpen function (Fig. 9c) was implemented to return an enhanced version

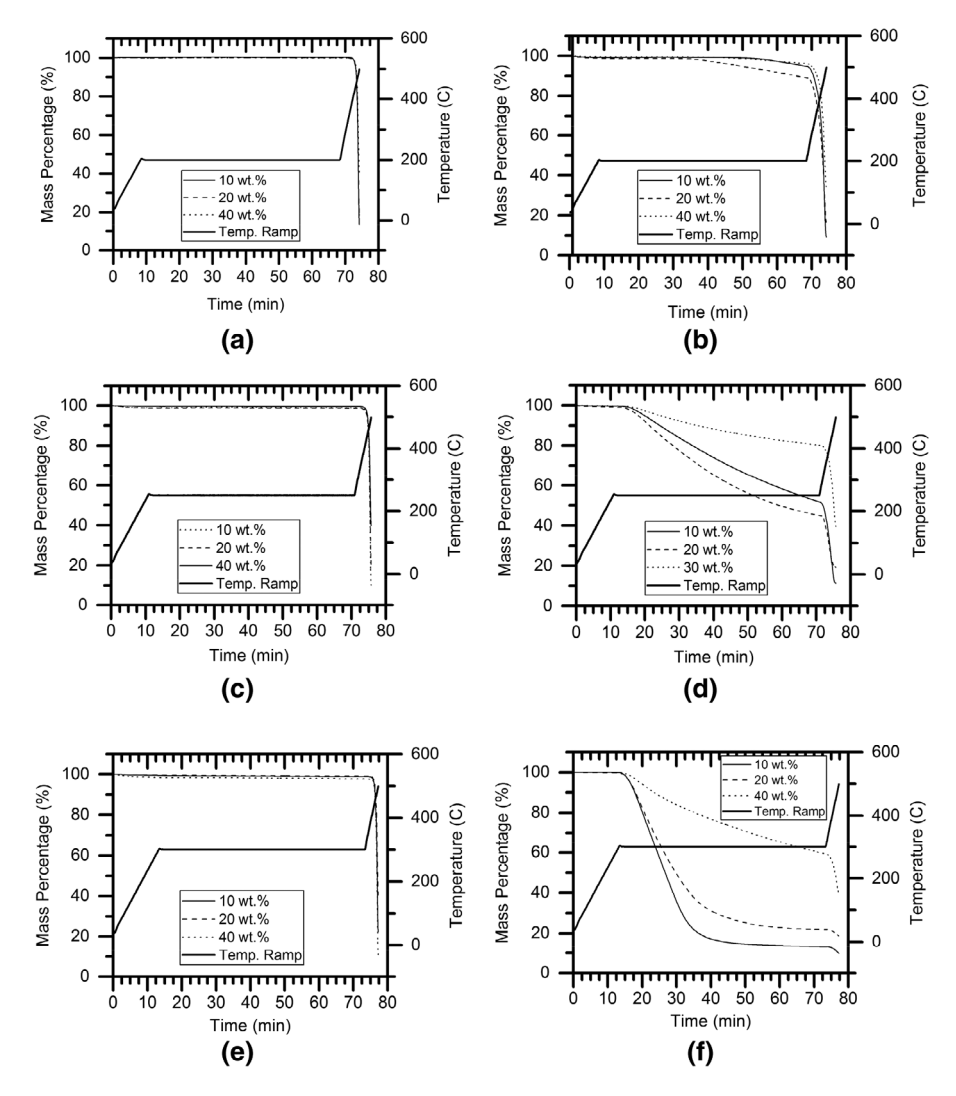


FIG. 8. Mass loss percentage and temperature ramp for (a) 200° C with N2, (b) 200° C with air, (c) 250° C with N2, (d) 250° C with air, (e) 300° C with N2, and (f) 300° C with air.

TABLE 3. Computed tomography parameters.

Parameter	Value
Voltage (KV)	70
Current (µA)	110
Integration Time (s)	1
Gain	8.0×
Image averaging	Off
Binning	1×1
Number of projections	1,800
Static grayscale correction	9,000-10,000

of the grayscale image. To convert the images to binary format, the roicolor function (Fig. 9d) was added to select the particles within an intensity range of 4.104 and 7.104 to standardize the process for all images. During the analysis of the images, it was found that voids (black dots) were presented inside the samples. To target the reason of this appearance, the bulk material (pellets) was scanned. Voids are present from the bulk state of the process (before extrusion process and injection molding process) and stay constant along the manufacturing process. For this reason, due to the presence of voids, a code was created to select sections of the image without voids. Afterwards, each section was united to create a single image. Because the image was converted to binary format, it was possible to distinguish between the GB particles and the PP matrix inside the code. A value of zero (0) was given to the polymer matrix and a value of one (1) to the particles to be able to compute the average volume fraction of particles within each row. Subsequently, the particle volume fraction as a function of the sample radial position was calculated and plotted.

RESULTS AND DISCUSSION

Feed Material (Pellets)

To ensure that the bulk material contains a homogeneous distribution of particles throughout the entire volume, pellets were scanned individually and analyzed. Pellets were scanned with a resolution of 8 µm to accurately view the particle size. Figure 10 shows the particle volume fraction as a function of radial position of the scanned pellet. For the material with 10 wt% GB, an average of 4.04 vol% GB was calculated using the MATLAB script. For the 20 and 40 wt% GB, an average of 6.56 and 13.94 vol% correspond, respectively. It is noteworthy to mention that as a result of the pre-existing voids, valleys in the plot are observed.

Using Eq. 1, the variation was calculated for all the volume fractions. For the material bearing 10 wt% GB, a variation of 6.05% was calculated. For the 20 and 40 wt% GB, a variation of 20 and 27.39% was calculated, respectively. Even though the variation is high for the 20 and 40 wt%

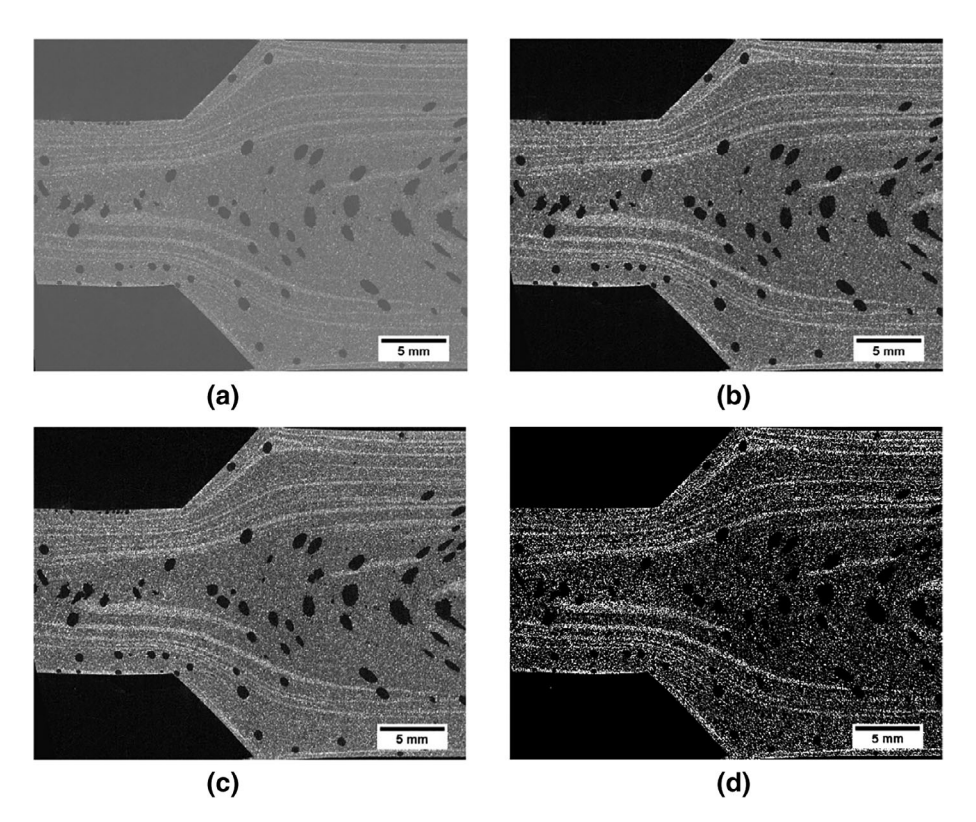


FIG. 9. Image processing steps where (a) import the image to the work-space, (b) adjust the intensity of the image gray-scale, (c) enhance the gray-scale of the imported image, and (d) select the intensity of interest converting the image into binary format.

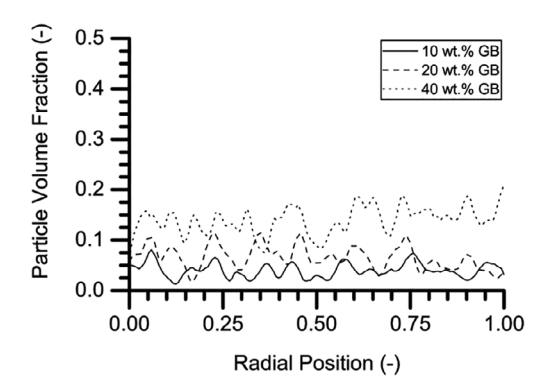


FIG. 10. Pellet particle volume fraction as a function of the radial position.

GB, the variation was found to vary depending on the portion of the image that was being analyzed. One source of error is the fact that not all particles are shown exactly at the middle. This leads to their volume fractions being under-represented. Some of the observed particles are located exactly in the cross-section of the center of the sphere. However, not all the particles show up in this position. It was found that the 2D representation was sufficient to describe the volume fraction in 3D space.

$$\% variation = \left| \frac{x_{exp} - x_{theory}}{x_{theory}} \right|$$
 (1)

Extrusion Process

Samples from the extrusion process were manufactured using PP with 10, 20, and 40 wt% GB. Sections in the extrudate, cone inlet, cone outlet, die inlet and die outlet were cut and analyzed.

Extrudate. Samples taken directly out of the extruder without the presence of the die, giving insight into the state of the material before it enters the die, were analyzed. The material was collected before entering the die. Figure 11 shows the extrudate for 20 wt% GB at 20 RPM. Voids with elongated shape can be seen inside the material. This elongation occurs as a result of the sample collecting method. As the extrudate leaves the extruder, gravity leads to an elongation of the material causing the voids inside the polymer to elongate.

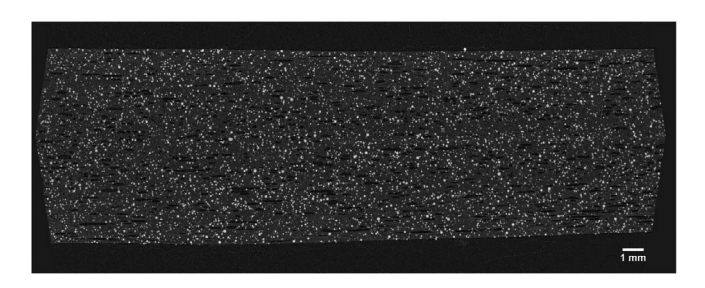


FIG. 11. CT Scan of extrudate material with 20 wt% GB at 20 RPM.

Results for the 10, 20, and 40 wt% distributions across the diameter of the extrudate are presented in Fig. 12. The graphs present measurements performed at three different concentrations, showing the upper limit, lower limit, and average fractions. The average was calculated using four different cross-sections of the same sample. PP with 10 wt % GB shows no variation of particle distribution over the diameter leaving the extruder. A concentration of 3.4 \pm 1 vol% was measured using the MATLAB script. When comparing the screw speed, no influence of particle distribution can be seen between 10 and 20 RPM. A similar effect was observed for 20 wt% GB, with slightly higher GB content near the outer surface, closer to the wall. The concentration of GBs is homogeneously distributed over most of the diameter of the sample with a value of 10.1 \pm 1.7 vol% for both screw speeds. Samples with 40 wt% GB displays a value of approximately 21.4 ± 2.3 vol%. Close to the walls, a higher concentration of particles is observed with a value of approximately 28 vol%. The peak close to the walls indicates a migration of particles toward the edges of the extruder, which seems to be dependent of the particle concentration. This behavior is seen for both screw speeds.

These results suggest that a filler-matrix de-mixing or separation occurs inside the screw, either during melting or in the metering or mixing zones of the screw. Further studies of the flow and particle migration in the screw extruder are needed to understand this phenomenon.

Cone. The extruder-to-die cone adapter was then analyzed. Samples were scanned before and after the cone adapter. An agglomeration of particles is observed in the center of the sample with slight accumulation at the cone walls. Figure 13 shows the results for the samples with 10 wt% GB. The outer layer of the inlet cone (close to wall) shows a particle volume density distribution of 39.4 vol%. Afterwards, a sudden level drop in distribution is observed with a value of 6.4 ± 1.8 vol% before increasing to a second maximum of 24.7 \pm 11.2 vol% of GBs particles. The outer layer of the cone outlet displays a value of 11.7 ± 2.5 vol%. The particle distribution decrease slightly to 6.5 \pm 1.5 vol% and increase to 12.3 \pm 11.3 vol% at the center of the flow. Results suggests a particle migration in the conical adapter towards the center and the walls during flow.

Die. Samples at the inlet and outlet of the customized die were analyzed. Once the flow reached steady state the flow was stopped by closing both valves at the ends of the die. Figure 14 shows the average particle density distribution for 10 wt% GB at 20 RPM. The higher concentration of particles are located close to the edges of the die (walls). The behavior observed is similar to the one in the cone adapter. Closest to the wall there is a peak of 35.8 \pm 11.7 vol% followed by a drop to 4.3 \pm 1.6 vol% and again another peak at the center of 7.7 \pm 3.6 vol%. At the outlet section of the die, the

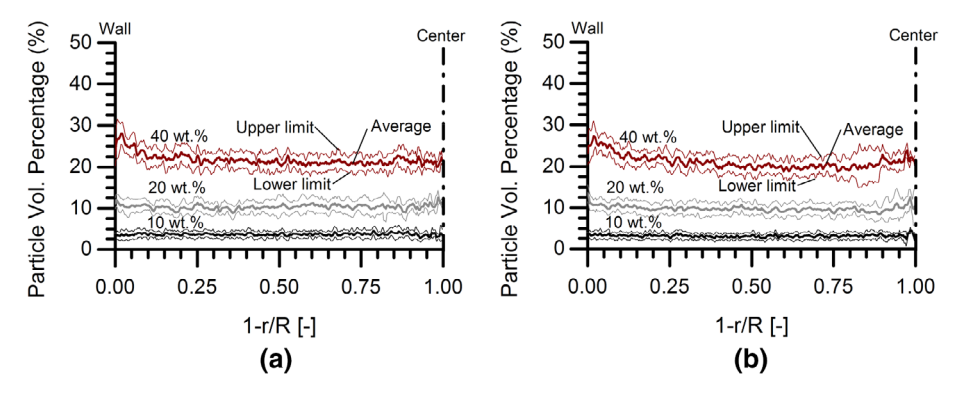


FIG. 12. Particle density distribution as a function of radial position for (a) 10 RPM and (b) 20 RPM. [Color figure can be viewed at wileyonlinelibrary.com]

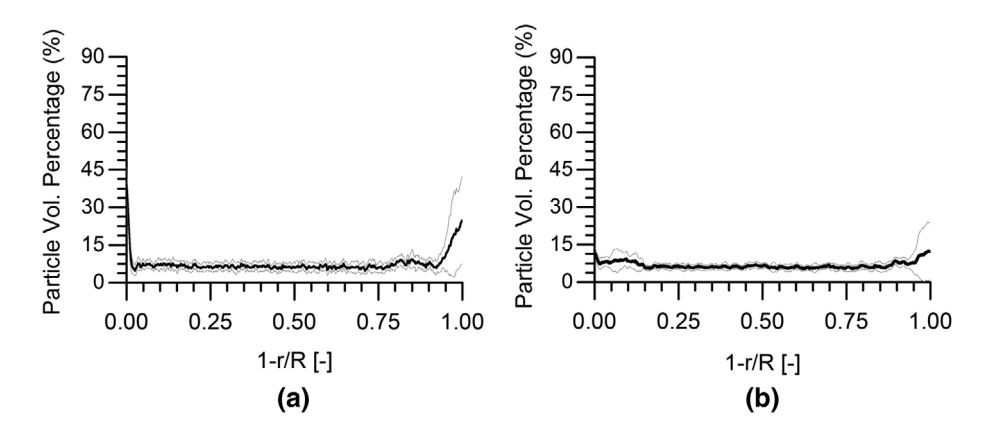


FIG. 13. Particle density distribution as a function of radial position of a 10 wt% GB for (a) before contraction and (b) after cone contraction.

concentration close to the walls is similar with a peak of 39.8 ± 12.8 vol% and follow the same behavior. For a screw speed of 20 RPM, again the same behavior is observed. A maximum close to the walls with a sudden drop and later an increase to the center of the flow is observed. For both screw speeds, an increase of particles can be seen from the inlet of the die to the outlet. This layer of particle has a thickness of about 0.1 mm with a particle concentration up to 800% higher than the average particle density distribution.

Samples with 20 and 40 wt% GB at 20 RPM exhibit an increase in particle density distribution near the wall of the die, from the inlet to the outlet of the die. A clear migration of particles to the walls is observed. This behavior is counter intuitive as a result of the movement of particles from the lower shear stress to the higher shear stress during flow. Since the velocity on the walls is assumed zero and almost zero next to the walls, the GBs remain at those locations. There could be a normal stress on the particles in the radial direction, allowing migration towards the walls. Samples at

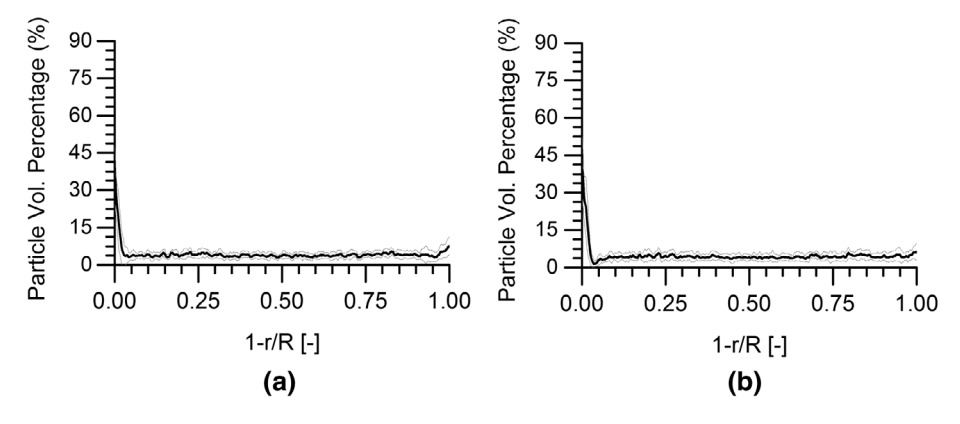
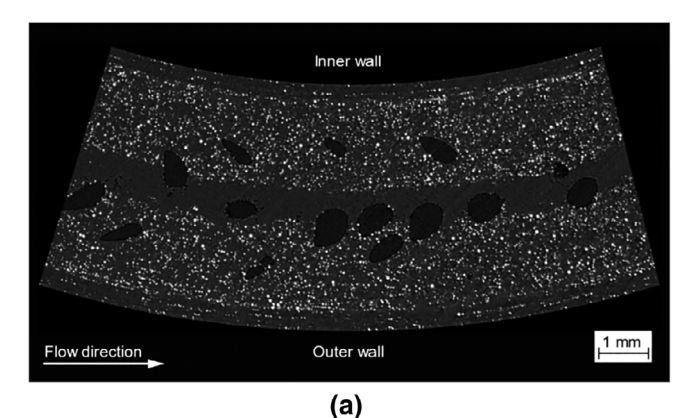
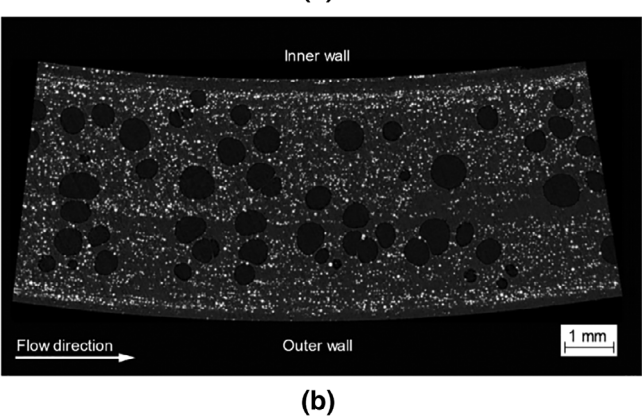


FIG. 14. Particle density distribution as a function of radial position of a 10 wt% GB for (a) inlet and (b) outlet of customized die.





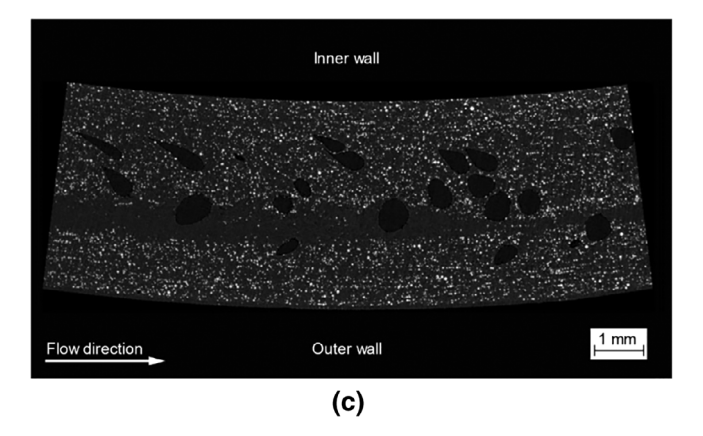


FIG. 15. 2D cross-sectional image for (a) close to sprue and opening of mold, (b) center, and (c) end of spiral mold.

10 RPM show similar behavior as samples at 20 RPM. Again, the maximum concentration of particles is located close to the walls with no visible migration at the center of the flow.

Injection Molding Process

Spiral mold samples were manufactured using PP with 20 and 30 wt% GB. A melting temperature of 280°C was used with a mold temperature of 80°C. The injection speed and injection volume used are 49.9 cm³/s and 20 cm³, respectively. The spiral was cut in lengths of 35 mm. Samples at the opening, center and end of the spiral mold were collected and analyzed.

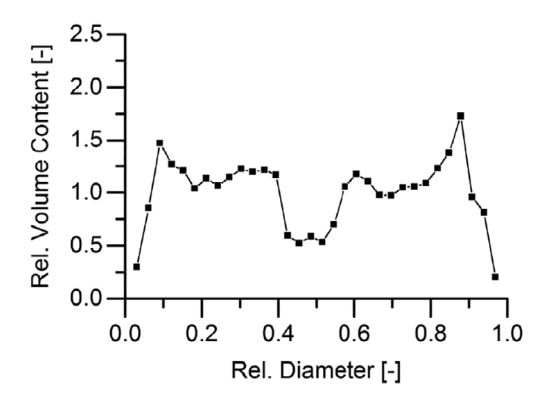


FIG. 16. Relative bead volume content for sample containing 20 wt% GB at the opening section of the spiral mold.

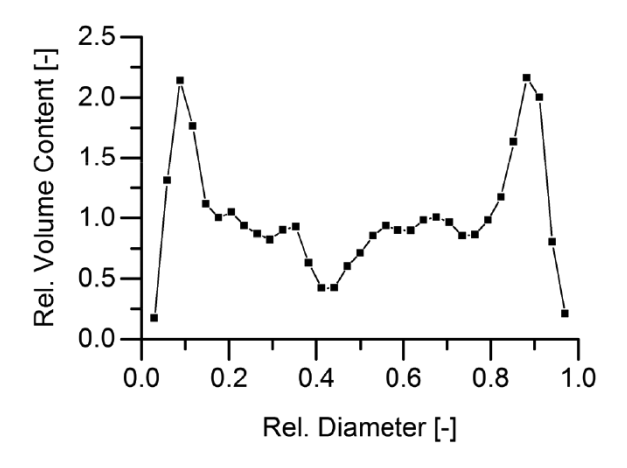


FIG. 17. Relative bead volume content for sample containing 20 wt% GB at the center of the spiral mold.

Opening of Spiral Mold. Figure 15a shows the particle distribution close to the sprue of the spiral mold. The spiral molded part can be categorized into four sections. The edge containing high matrix content followed by a peak with high particle content, a transition area and the core with mostly matrix material. Voids are detected at the core and transition area of the spiral molded parts. Figure 16 shows the particle density distribution where 0 describes the outer wall of the mold and 1 the inner wall. The distribution of

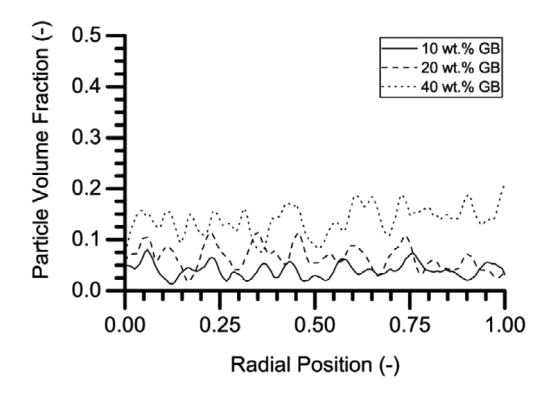


FIG. 18. Relative bead volume content for sample containing 20 wt% GB at the end of the spiral mold.

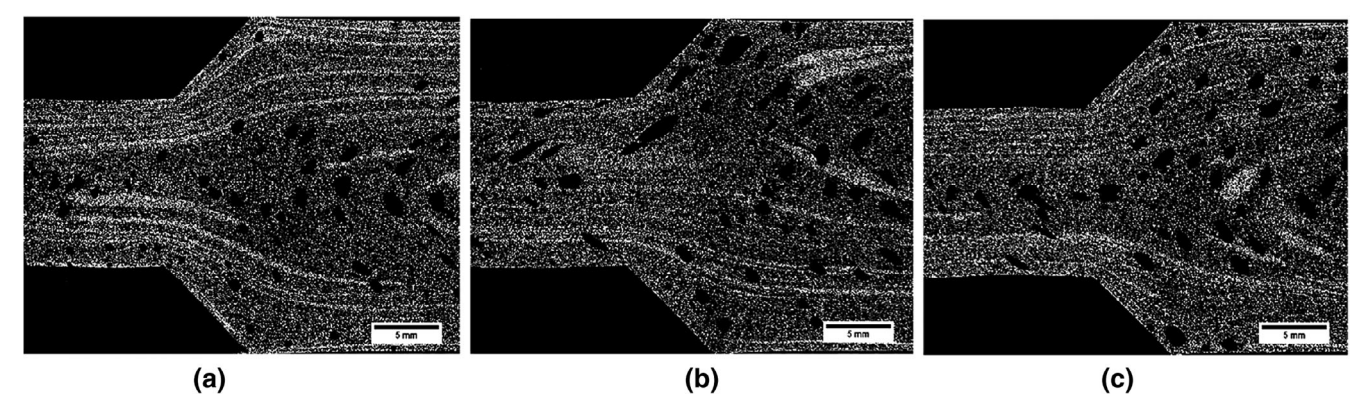


FIG. 19. (a) Sprue sketch and (b) cross-sectional image of the sprue zone. [Color figure can be viewed at wileyonlinelibrary.com]

particles is symmetrical. The highest amount of particles are located at 0.1 and 0.9. These peaks are followed by a consistent distribution of particles until the core section, which has the lowest particle content.

Center of Spiral Mold. Figure 19b shows the particle distribution at the center of the spiral mold. The matrix width at the outer edges decreased from 16 to 10%. Higher concentration of particles are located at the inner wall of the mold. However, this concentration is not seen at the outer wall. The core area decreased in width and is moved to the outer wall. The distribution of particles in Fig. 17 shows that the peak is larger compared with the opening of the mold. The transition and core sections width are reduced. Additionally, higher quantity of voids are present in this position.

End of Spiral Mold. Figure 15c shows the particle distribution at the end of the spiral mold. The width of the rich matrix area close to the inner walls decreased following the same behavior as at the center of the mold. At this position the edges are filled with particles as shown in Fig. 18. The transition area becomes wider while the core width increases compared with the center section of the mold. The core continues to drift towards the outer wall of the spiral mold. Some observed characteristics of the discontinuous process are that the edges contain only matrix material at the beginning of the flow and become thinner

with increasing flow path. A particle-free section along the axis will drift to the outer wall. Higher concentration of particles next to the matrix area is located at the opening and center but not at the end of the mold. During flow, this particle concentration moves to the edges filling this section along the flow path and having a more homogeneous distribution in the mold cavity.

Sprue. To understand the behavior of the particles at the opening section of the mold, a small sample of the sprue containing 30 wt% GB was cut and analyzed as shown in Fig. 19a. The sample is located close to the nozzle of the plasticizing unit. Figure 19b shows the polymer stream already appears at the opening of the sprue with similar particle position as Fig. 15a. The origin of the filler–matrix separation occurs during the plasticization process inside the barrel or during the injection process through the nozzle. This effect suggests that particle-matrix separation already occurs in the plasticizing unit of the injection molding machine, similar to the phenomena observed in the extrusion process.

Screwless Extruder

Samples from the screwless extruder were manufactured using PP with 20 wt% GB. Three pressure levels were used to study the particle migration at different processing

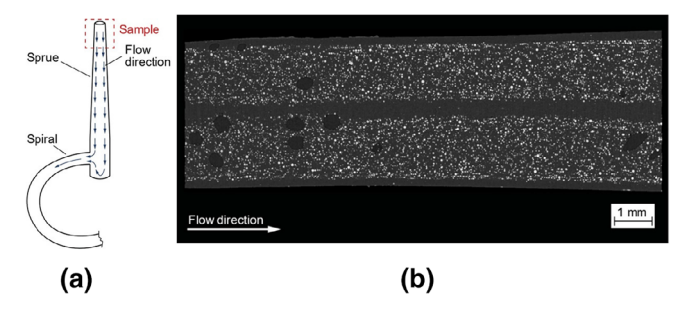


FIG. 20. Image processing of cone under isothermal conditions at (a) 344.7 kPa, (b) 517.1 kPa, and (c) 689.5 kPa (50, 75 and 100 psi) for 20 wt% GB. The flow direction moves from largest to smallest diameter. [Color figure can be viewed at wileyonlinelibrary.com]

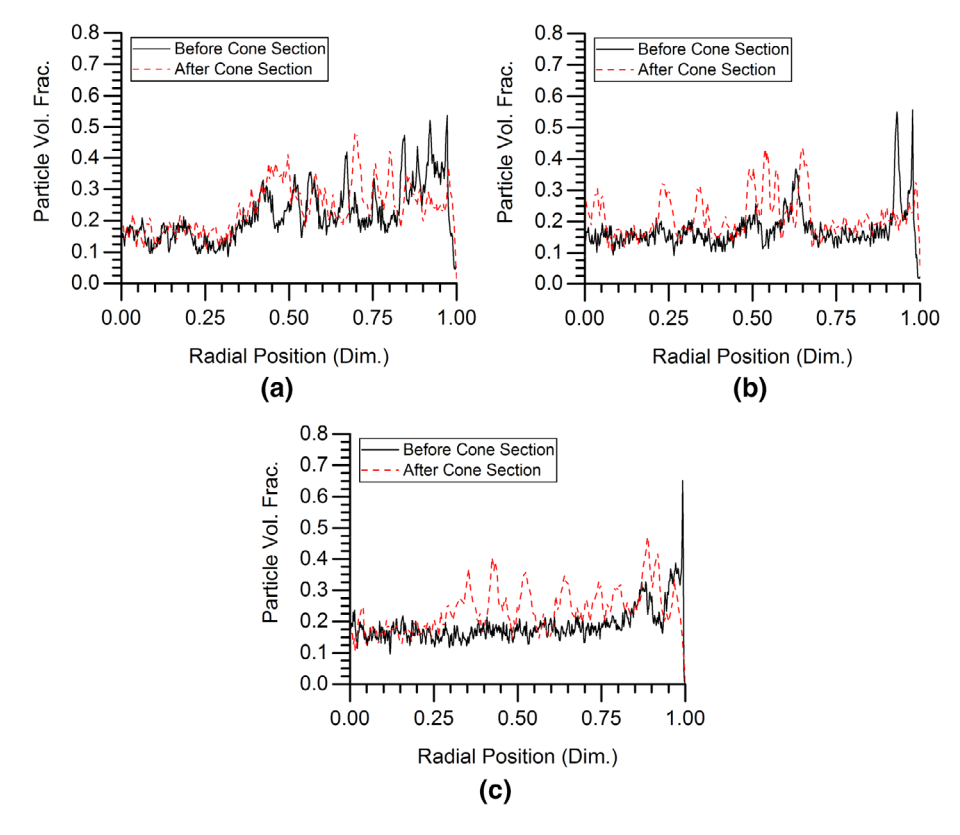


FIG. 21. Particle density distribution (φ) for a 20 wt% GB before and after conical contraction at (a) 344.7 kPa (50 psi), (b) 517.1 kPa (75 psi), and (c) 689.5 kPa (100 psi). [Color figure can be viewed at wileyonlinelibrary.com]

speeds. The experiments were performed under isothermal conditions.

Cone Section. Once the polymer was injected through the cone and solidified, the samples inside the cone section were cut and analyzed. The cone section was scanned with a resolution of 19.67 µm. Because the resolution of the scanned section is close to the size of the particles (25–50 µm), the size of the particles is not accurate. Even though the resolution of the scanned sections are close to the particle size, the images show a clear behavior and concentration of the particles. Figure 20 shows the scanned cone section for isothermal conditions for a 20 wt % GB sample. A more complete study incorporating the 10 and 40 wt% GB and nonisothermal conditions will be published at a later date. Isothermal condition means that all sections (barrel, cone and die) have the same temperature (205.4°C).

As shown in Fig. 20, migration and agglomeration of particles along the flow stream lines can be seen for samples with 20 wt% GB under isothermal conditions. Figure 21 shows the particle volume fraction as a function of the radial position. Peaks along the radial position can be observed closer to the wall of the conical section. These peaks suggest that particles are migrating and flowing towards the wall in chains. The anisotropic distribution of particles between the two wall sides is as a result of the

horizontal position of the experimental setup. The higher concentration of particles is located at the bottom part of the samples. These chain formations are produced by the lift effects after initiating flow of the material.

Figure 21a shows the particle density distribution at 344.7 kPa (50 psi). Accumulation of particles can be seen closer to the walls. The distribution of particles is wider compared with 517.1 kPa (75 psi) and 689.5 kPa (100 psi). For a pressure of 344.7 kPa, the peak concentrations maintain their position through the contraction. For a pressure of 517.1 and 689.5 kPa, the same behavior can be observed for most of the peaks in the form of particle chains. However, the concentration increases at the cone outlet compared with the particle density distribution at the cone inlet. For samples with 20 and 40 wt% formation of particle chains can be inferred as a result of the peak formation after the cone contraction.

Discussion

All three experimental set-ups show the same migration pattern, particles are migrating towards the walls. Liu and Joseph observed similar behavior [40]. Their experiment of sedimentation of particles in polymer solutions suggest that extensional stresses control the properties of aggregation of particles in viscoelastic fluids. It is clear that the fluid dynamics of sphere-wall interactions play a significant role in the

anomalous rolling of spheres as a result of the hydrodynamic forces. During an argument Joseph suggested that the viscoelasticity of the fluid could change the sign (positive/negative) of the effective pressure, the first normal stress at the front of the stagnation point. This change in sign might produce the pull required for wall-sphere interaction. A similar explanation was given by Laun [31], where he proposed that the first and second normal stresses have negative and positive magnitude for a viscoelastic material, respectively.

Huang et al. [16] performed direct simulation of the sedimentation of elliptic particles in Oldroyd-B fluid. Oldroyd-B fluids present one of the simplest models capable of describing the viscoelastic behavior of dilute polymeric solutions [41]. They showed that the normal component of the extra stress on a rigid body vanishes and the lateral forces and torques are determined by the pressure. In viscoelastic fluids, long bodies are formed by spheres that are under the kissing phenomenon are stable to turning couples when long bodies aligned along the stream. He mentioned that these normal stresses are compressive and give rise to high pressure when the flow is fast, following the explanation given by Laun [31]. The migration and orientation of particles are controlled in slow flow by compressive normal stresses, which are large where the shear rates are large. Subsequently, compressive normal stresses cause particles to line up, straighten out, and aggregate forming chains. Because the orientation of the particle varies from Newtonian to Non-Newtonian fluid, the migration of particles is determined by a competition between the normal stresses due to inertia and viscoelasticity (Reynold's number). For our experiments, particles are immersed in a Non-Newtonian matrix under very small Reynold's number.

Huang et al. [13] performed direct simulation of motion of neutrally and non-neutrally buoyant particles in viscoelastic fluids. They determined that the equilibrium position of neutrally buoyant particles depends on the inertia, elasticity, shear thinning behavior of the polymer and the blockage ratio (size of particle divided by the size of the channel). They found that the migration of particles is controlled by elastic normal stresses that are limited by slow flows in two dimensions, which are compressive and proportional to the square of the shear rate on the body. However, normal stresses are not the only forces, which can cause particle migration in a shear-thinning fluid according to Huang. A lateral imbalance of the shear stress can also cause lateral migration. Additionally, they observed that the effects of viscoelastic stresses are modulated by the wall blockage. A particle experiences an attraction towards the nearby wall at large blockage ratio, but moves towards the center at small blockage ratios.

However, due to the small particles embedded in the PP matrix the opposite is happening in our experiments as a result of the compressive normal stresses of the viscoelastic fluids. Huang discovered that the particles come closer to the wall as the power law index (n) decreased. In an experiment performed by Ko et al. [33] it was found, that the hydrodynamic lift force balances the buoyant weight of heavier particles in a channel. They found that the normal

stress effects enhance the lift of particles. During an experiment with a horizontal channel, they found that there is an equilibrium position for heavy particles. These equilibrium positions are a function of the Reynold's number and particle size. These experiments were performed with a channel Reynold's number between 1 and 250. For Oldroyd-B fluids, a Reynold's number between 1 and 30 was used for the simulations performed by Ko et al. At high Reynold's number the particles migrate to the center while at low values (Re < 1) they migrate to the walls. Even though our Reynold's numbers are within a magnitude of 10^{-5} to 10^{-8} , these positions agree with our findings shown in Fig. 20 for the screwless extruder observed for 20 wt% GB, extrusion process and injection molding process.

An explanation for this phenomenon could be the existence of a negative first normal stress difference $N_1 = -|\tau|$ and a second positive normal stress difference $N_2 = -\frac{1}{2}N_1$, as suggested by Laun et al. [31]. Unlike Morris and Boulay [26], who developed an equation to describe shear induces migration of particle in a Newtonian fluid to low shear rate region, Laun describes this movement in the opposite direction, radially towards the walls.

CONCLUSION

Computed tomography was used to study the particle migration of GBs during different manufacturing processes. For the extrusion process, extrudate showed an even distribution of particles. At the conical adapter, particles move to the wall and center of the cone outlet. In the customized die, a higher concentration of particles at the wall was observed at the outlet compared with the inlet. This higher concentration of particles suggests migration of particles towards the wall. For the injection molding process of the spiral mold, significant filler-matrix separation was observed. At the opening section of the mold, the edge is nearly bead-free. This particle-matrix separation can already be seen in the sprue section, which suggests that migration already occurs in the plasticizing unit. The matrix core drifts along the flow path to the outer wall of the mold. As the polymer flows through the die, particles migrate to the center and the walls of the mold filling the bead-free edge seen at the opening. For the screwless extruder, a lift effect of the particles is occurring. Long chains of particles aggregate at different radial positions. This aggregation suggests that an equilibrium position is obtained in direction towards the wall as a result of the viscoelastic stresses. For all three processes, the shear thinning behavior of the material and the effects of the viscoelastic stresses are forcing the particles to the walls along the flow. It is suggested and supported by literature [42,43], that no matter the initial position of the particle, it will migrate and obtain a final position towards the wall.

A more complete study incorporating the 10 and 40 wt % GB and non-isothermal conditions for the screwless process will be published at a later date.

FUTURE WORK

Future work consists of repeating the experiments with different die dimensions. Different polymer matrices and fillers will also be tested. To increase the packing density of the pellets it is suggested to grind the material into smaller pellets or into powder. By doing this, the air pockets in the solidified matrix can be reduced. Fiber-filled materials are of interest to study fiber orientation during a contraction.

ACKNOWLEDGMENT

The authors thanks Teel Plastic Inc. for their technological and financial support in this project.

REFERENCES

- S. Goris, J. Puentes, and T. A. Osswald. "Polymer-Composites Manufacturing Processes," in *Manufacturing Engineering Handbook*, Chapter 34. 2nd edition. McGraw-Hill, New York.
- C. Kuhn et al., J. Compos. Sci. 2(1), 2 (2018). DOI: 10.3390/jcs2010002.
- 3. S. Goris and T.A. Osswald. *Composites Part A: Applied Science and Manufacturing* **105**, 321 (2018).
- 4. M.M. Villone et al., Computers and Fluids, 42(1), 82 (2011).
- D. Semwogerere, J.F. Morris, and E.R. Weeks, *Journal of Fluid Mechanics*, 581, 437 (2007).
- D. Semwogerere and E.R. Weeks, *Physics of Fluids*, 20, 043306 (2008). DOI:10.1063/1.2907378
- 7. G. Segré and A. Silberberg, Weizmann Institute of Science, 14(1), 136 (1962).
- 8. R.J. Phillips, R.C. Armstrong, and R.A. Brown, *Physics of Fluids*, **4**(1), 30 (1992).
- 9. H.H. Hu and D.D. Joseph, *Theoretical and Computational Fluid Dynamics*, **3**, 285 (1992).
- P.R. Nott and J.F. Brady, *Journal of Fluid Mechanics*, 275(1994), 157 (1994).
- 11. J. Feng, H.H. Hu, and D.D. Joseph, *Journal of Fluid Mechanics*, **261**, 95 (1994).
- 12. J. Feng, H.H. Hu, and D.D. Joseph, *Journal of Fluid Mechanics*, **277**, 271 (1994).
- 13. P.Y. Huang et al., Journal of Fluid Mechanics, 343, 73 (1997).
- 14. M.S. Ingber et al., *International Journal of Multiphase Flow*, **35**(3), 270 (2009).
- 15. A. Kumar and M.D. Graham, *Physical Review Letters*, **109**(10), 1 (2012).
- P.Y. Huang, H.H. Hu, and D.D. Joseph, *Journal of Fluid Mechanics*, 362, 297 (1998).

- 17. Y.J. Liu et al., Journal of Non-Newtonian Fluid Mechanics, **50**, 305 (1993).
- 18. A.F. Fortes, D.D. Joseph, and T.S. Lundgren, *Journal of Fluid Mechanics*, **177**, 467 (1987).
- 19. P. Aarts et al., Arteriosclerosis, 8(6), 819 (1988).
- 20. J.R. Abbott et al., Journal of Rheology, 35(5), 773 (1991).
- P. Mills and P. Snabre, In: Journal of Physics II, 5(10), 1597 (1995).
- 22. J. Morris and J. Brady, *In: International Journal of Multiphase Flow*, **24**(1), 105 (1998).
- D. Leighton and A. Acrivos, Journal of Fluid Mechanics, 181, 415 (1987).
- 24. A. W. Chow, S. W. Sinton, and J. H. Iwamiya, *Phys. Fluids* **6**(8), 2561.
- 25. L.A. Mondy et al., Journal of Rheology, 38(2), 444 (1994).
- J.F. Morris and F. Boulay, *Journal of Rheology*, 43(5), 1213 (1999).
- 27. L. Elias et al., J Polym. Sci. Part B. 46(18), 1976 (2008).
- 28. A. Goldel et al., *Macromolecules* **44**(15), 6094 (2011).
- 29. T. Gong et al., Polymer 110, 1 (2017).
- 30. L. Bai et al., Langmuir 34(3), 1073 (2018).
- 31. H.M. Laun, J. Non-Newtonian Fluid Mech., 54, 87 (1994).
- 32. F. Gauthier, H.L. Goldsmith, and S.G. Mason, *Transactions of the Society of Rheology*, **15**(2), 297 (1971).
- 33. T. Ko, N.A. Patankar, and D.D. Joseph, *Computers and Fluids*, **35**, 121 (2006).
- 34. E.C. Eckstein, A.W. Tilles, and F.J. Millero, *Microvascular Research*, **36**(1), 31 (1988).
- 35. A. Tilles and E. Eckstein, *Microvascular Research*, **33**(2), 211 (1987).
- 36. M. Frank et al., Journal of Fluid Mechanics, 493, 363 (2003).
- 37. I.E. Zarraga, D.A. Hill, and J.D.T. Leighton, *Journal of Rheology*, **45**(5), 1065 (2001).
- 38. C. Rauwendaal. Polymer Extrusion. Hanser Publications (2014).
- L. Shibryaeva. Thermal Oxidation of Polypropylene and Modified Polypropylene Structure Effects, Polypropylene Fatih Dogan, IntechOpen, DOI:10.5772/34388. Available from: https://www.intechopen.com/books/polypropylene/thermal-oxidation-of-polypropylene-and-modified-polypropylene-structure-effects
- 40. Y.J. Liu and D.D. Joseph. *Journal of Fluid Mechanics* **255**, 565 (1993). DOI:10.1017/S0022112093002599.
- Application Gallery: "Flow of Oldroyd-B Viscoelastic Fluid." COMSOL, www.comsol.com/model/flow-of-oldroyd-b-viscoelastic-fluid-4383.
- 42. G. D'Avino et al., Computers and Fluids, 42, 82 (2009).
- 43. G. D'Avino et al., *Journal of Non-Newtonian Fluid Mechanics*, **165** 466 (2010).